nature communications

Article

https://doi.org/10.1038/s41467-025-61884-x

Coherence in resonance fluorescence

Received: 14 May 2024

Accepted: 4 July 2025

Published online: 12 July 2025

Check for updates

Xu-Jie Wang[1], Guoqi Huang[1,2], Ming-Yang Li[3], Yuan-Zhuo Wang[3], Li Liu[1], Bang Wu[1] ✉, Hanqing Liu[4,5], Haiqiao Ni[4,5], Zhichuan Niu[4,5], Weijie Ji[1], Rongzhen Jiao[2], Hua-Lei Yin[1,3,6] ✉ & Zhiliang Yuan[1] ✉

Resonance fluorescence of a two-level emitter displays persistently anti-bunching irrespective of the excitation intensity, but inherits the driving laser's linewidth under weak monochromatic excitation. These properties are commonly explained in terms of two disjoined pictures, i.e., the emitter's single photon saturation or passively scattering light. Here, we propose a unified model that treats all fluorescence photons as spontaneous emission, one at a time, and can explain simultaneously both the spectral and correlation properties of the emission. We theoretically derive the excitation power dependencies, measurable at the single-photon incidence level, of the first-order coherence of the whole resonance fluorescence and super-bunching of the spectrally filtered, followed by experimental confirmation on a semiconductor quantum dot micro-pillar device. Furthermore, our model explains peculiar coincidence bunching observed in phase-dependent two-photon interference experiments. Our work provides an intuitive understanding of coherent light-matter interaction and may stimulate new applications.

Although being a textbook phenomenon[1–4], resonance fluorescence (RF) continues to be an active research topic even in its simplest form[5–11], where a two-level emitter (TLE) under weak monochromatic excitation scatters out photons that are anti-bunched and yet exhibit the driving laser's linewidth[12–16]. While both phenomena can be calculated by the unwavering formalism of light-atom interaction[1–4], confusion remains in their interpretations. Usually, anti-bunching is interpreted in the single-photon picture[17,18], where a TLE absorbs and re-emits photons one at a time. However, this picture fails to account for the RF's linewidth, which is far narrower than the natural broadening ($\frac{1}{2\pi T_1}$) imposed by the emitter's radiative lifetime (T_1). Conversely, it is easy to explain the laser-like spectrum if one treats the TLE only as a passive scattering site[19], but explaining consistently the single-photon characteristic becomes challenging.

Accompanying the spectrally sharp peak, RF spectrum of a TLE contains also a broadband component, which is vanishingly insignificant under weak excitation (Heitler regime) but grows towards dominance and eventually develops into Mollow triplets under strong excitation[20]. Recently, López Carreño et al.[5] theoretically clarified that the broadband component, however insignificant it may be, that holds the key to the presence or disappearance of anti-bunching through interference with the laser-like spectral component. Drastically departing from the single-photon picture, the broadband component was attributed to higher-order scattering processes involving "the actual two-photon absorption and re-emission"[5,9], which prompted experiments on the spectral filtering's effect on the photon number statistics[6–8] and even led to suggestion of simultaneous scattering of two photons by an atom[8]. However, spectrally resolving the RF invokes interference among (many) photons emitted over a macroscopic duration no less than $1/\Delta\nu$ ($\Delta\nu$: spectral resolution), which would prevent discerning what truly happens at the minuscule duration of the TLE's radiative lifetime. From the perspective of wave-particle duality, the action of filtering reveals already the wave-aspect properties, and thus undermines

[1]Beijing Academy of Quantum Information Sciences, Beijing, China. [2]School of Science, Beijing University of Posts and Telecommunications, Beijing, China. [3]National Laboratory of Solid State Microstructures and School of Physics, Collaborative Innovation Center of Advanced Microstructures, Nanjing University, Nanjing, China. [4]State Key Laboratory of Optoelectronic Materials and Devices, Institute of Semiconductors, Chinese Academy of Sciences, Beijing, China. [5]Center of Materials Science and Optoelectronics Engineering, University of Chinese Academy of Sciences, Beijing, China. [6]School of Physics and Beijing Key Laboratory of Opto-Electronic Functional Materials and Micro-Nano Devices, Key Laboratory of Quantum State Construction and Manipulation (Ministry of Education), Renmin University of China, Beijing, China. ✉e-mail: wubang@baqis.ac.cn; hlyin@ruc.edu.cn; yuanzl@baqis.ac.cn

discussions on simultaneity which requires treating photons as particles.

In this work, we propose and experimentally verify a unified model which simultaneously explains the laser-like linewidth and the single-photon characteristics of the RF of a quantum emitter. The model involves no higher-order scattering processes, nor does it need to distinguish between "coherent" scattering and "incoherent" absorption/re-emission processes. Here, all RF photons are strictly treated as spontaneous emission, one at a time and never two together. We theoretically derive the excitation power dependencies, with the strongest effects measurable at the single-photon incidence level, of the first-order coherence ($g^{(1)}$) of the RF as whole and the second-order correlation function ($g^{(2)}$) of its broadband component. In laboratory, we confirm the model by reproducing its predictions on the RF from a high-quality semiconductor quantum dot (QD) micropillar device.

Results

Pure-state model for resonance fluorescence and its predictions

Figure 1a depicts the spontaneous emission model. A monochromatic laser coherently drives a TLE, e.g., a QD in a micropillar cavity[11]. Parameters ν, $h\nu$ and T_L are the laser's frequency, photon energy and coherence time, respectively. The TLE's excited state $|e\rangle$ has a lifetime of T_1, and a dephasing time of T_2 ($T_2 \le 2T_1$). According to the optical Bloch equations, the TLE population reaches a steady state after ~ T_1 time under steady continuous optical excitation[4]. Fundamentally, the TLE or its emission separately is in a mixed state. However, treating them jointly, it is possible, as derived in Section I, Supplementary Information, to use a pure-state description:

$$|\psi\rangle_t = \sqrt{p_0}|0\rangle_t|g\rangle_t + \sqrt{p_1}e^{-i2\pi\nu t}\frac{|0\rangle_t|e\rangle_t + |1\rangle_t|g\rangle_t}{\sqrt{2}}, \quad (1)$$

where $\sqrt{p_0}$ and $\sqrt{p_1}$ represent the magnitudes of the quantum probability amplitudes ($p_0 + p_1 = 1$). Here, $|0\rangle_t|e\rangle_t$ means the TLE occupying its excited state has not spontaneously emitted at time t, while $|1\rangle_t|g\rangle_t$ indicates emission of a photon has just taken place with the TLE having returned to its ground state $|g\rangle_t$. States $|0\rangle_t|e\rangle_t$ and $|1\rangle_t|g\rangle_t$ are connected only via spontaneous emission, and $|1\rangle_t$ represents a spontaneously emitted photon at t contributing to the RF. By definition, $|1\rangle_t$ is a broadband photon with bandwidth governed by the TLE's dephasing time T_2. The state $\frac{|0\rangle_t|e\rangle_t + |1\rangle_t|g\rangle_t}{\sqrt{2}}$ implies that, at any given instant of time, it is not possible to know whether spontaneous emission has taken place or the TLE remains at its excited state $|e\rangle$ prior to detection of a photon. However, once an RF photon is detected, we know for sure that spontaneous emission had taken place and the TLE returned to its ground state $|g\rangle$ at the corresponding instant of time. An immediate detection of a second photon is prevented because the TLE requires time to be repopulated. This leads naturally to photon anti-bunching.

Figure 1b shows an asymmetrical Mach-Zehnder interferometer (AMZI) suitable to evaluate the RF's coherence. The AMZI's delay (τ) is chosen to be much longer than the TLE relaxation time, but much shorter than the coherence time of the excitation laser, i.e., $T_1 \ll \tau \ll T_L$, so as to ensure the steady-state, and phase-coherent, condition. The

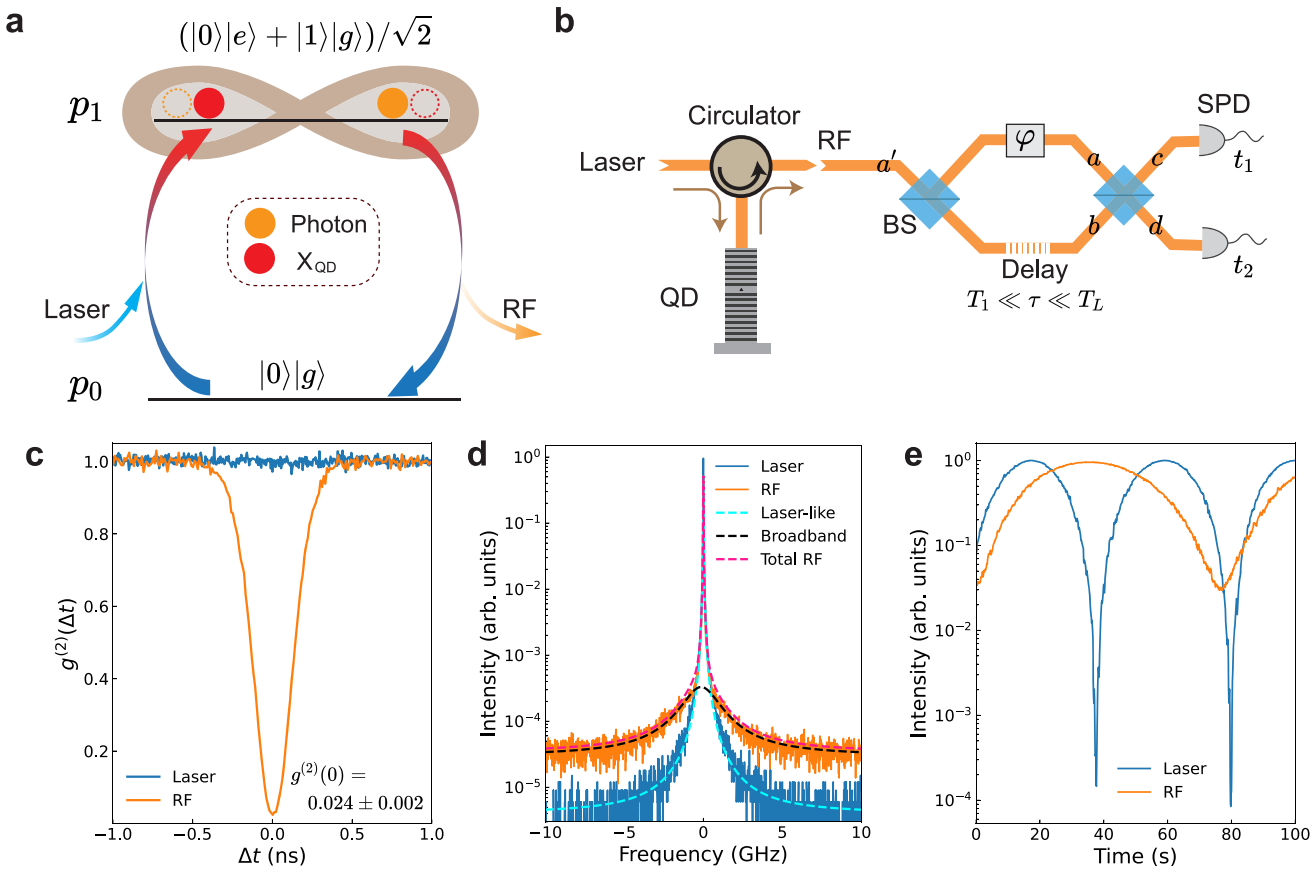

Fig. 1 | Resonance fluorescence (RF). a Schematic for a two-level emitter (TLE) coherently driven by a continuous-wave laser into steady-state. Brackets $|g\rangle$ and $|e\rangle$ represent the ground and excited states of the TLE, while $|0\rangle$ and $|1\rangle$ mean 0 or 1 spontaneously emitted photon. Symbols p_0 represents the population of the system ground state while p_1 is the single-quanta population that is in a form of either the TLE staying at its excited state ($|0\rangle|e\rangle$)) or a fresh spontaneously emitted photon ($|1\rangle|g\rangle$). **b** Schematic of the core experimental setup. The RF is collected in the same polarisation as the excitation laser. **c** Second-order correlation function $g^{(2)}(\Delta t)$ measurement traces. **d** High resolution spectra. **e** Interference fringes measured with the AMZI shown in (**b**). In this measurement we left the AMZI's phase φ drift freely and recorded the count rate of the SPDs as a function of elapsed time. BS beam splitter, SPD single-photon detector.

incoming RF signal from port a' is divided equally into two paths (a and b) by the first beam splitter and then recombine at the second one before detection at ports c and d by two single-photon detectors. When a photon is detected, it is not possible to distinguish whether the photon arose from the one emitted to an early time ($t-\tau$) taking the long path or one emitted at a late time (t) taking the short path. Interference between the two indistinguishable paths occurs. As the coherence properties of an RF signal is unaffected by channel losses (see Section II, Supplementary Information), we can then use the pure-state of Eq. (1) as the input to analyse the interference outcome after the AMZI. The AMZI output state can be written as:

$$\begin{aligned}|\Psi_{\text{out}}\rangle = |0_c 0_d\rangle_t &\left(p_0|gg\rangle + \frac{\sqrt{p_0 p_1}}{\sqrt{2}}|ge\rangle + \frac{\sqrt{p_0 p_1}}{\sqrt{2}}|eg\rangle + \frac{p_1}{2}|ee\rangle\right)\\ &+ |1_c 0_d\rangle_t \frac{\sqrt{p_0 p_1}}{\sqrt{2}}\frac{1-e^{i\varphi}}{\sqrt{2}}|gg\rangle + |1_c 0_d\rangle_t \frac{p_1}{2\sqrt{2}}\left(|ge\rangle - e^{i\varphi}|eg\rangle\right) - |2_c 0_d\rangle_t e^{i\varphi}\frac{p_1}{2\sqrt{2}}|gg\rangle\\ &+ |0_c 1_d\rangle_t \frac{\sqrt{p_0 p_1}}{\sqrt{2}}\frac{1+e^{i\varphi}}{\sqrt{2}}|gg\rangle + |0_c 1_d\rangle_t \frac{p_1}{2\sqrt{2}}\left(|ge\rangle + e^{i\varphi}|eg\rangle\right) + |0_c 2_d\rangle_t e^{i\varphi}\frac{p_1}{2\sqrt{2}}|gg\rangle,\end{aligned} \tag{2}$$

where φ denotes the AMZI phase delay and $|xy\rangle$ ($x, y = g, e$) represents the TLE's respective states corresponding to time bins $t-\tau$ and t. The first line contains no photons while the second and third lines represent photon outputs at ports c and d, respectively. Each output contains one phase-dependent term followed by two phase-independent ones. The phase-dependent term corresponds to the TLE's transition $(|ge\rangle + |eg\rangle)/\sqrt{2} \rightarrow |gg\rangle$, which imparts the coherence to a superposition between two photon temporal modes: $(|0\rangle_{t-\tau}|1\rangle_t + |1\rangle_{t-\tau}|0\rangle_t)/\sqrt{2}$. Varying the AMZI phase φ, this superposition will produce interference fringes with an amplitude of $\frac{p_0 p_1}{2}$, as opposed to the total output intensity of $\frac{p_1}{2}$. Thus, the coherence level of the RF, quantified using the first-order correlation function $g^{(1)}(\tau)$, has the form,

$$g^{(1)}(\tau) = p_0 e^{-i2\pi\nu\tau}. \tag{3}$$

Using Fourier transform, we infer that the RF consists of a spectrally sharp, laser-like (ll) part that inherits the linewidth of the driving laser and has a spectral weight of $I_{ll}/I_{tot} = |g^{(1)}(\tau)| = p_0 < 1$. For detailed theoretical derivation, see Sections II–IV, Supplementary Information.

The reduction in coherence, by the amount of $1-p_0$ or p_1, is linked to the TLE's transitions from the $|ee\rangle$ state to $|ge\rangle$, $|eg\rangle$ or $|gg\rangle$. As shown in Eq. (2), the first two transitions give rise to an incoherent single photon each while the last one produces a two-photon state. Transition $|ee\rangle \rightarrow |ge\rangle$ ($|ee\rangle \rightarrow |eg\rangle$) emitted a photon into early (late) temporal mode but none at late (early) mode, so no two-path interference takes place. On the other hand, transition $|ee\rangle \rightarrow |gg\rangle$ produces one photon into each mode, the interference of which causes coalescence and forms a photon-pair through Hong-Ou-Mandel (HOM) effect[21]. All these photons are incoherent, so they naturally display a bandwidth governed by the TLE's transition and thus make up the broadband (bb) part, with a weight of $I_{bb}/I_{tot} = p_1$ in the RF spectrum.

In the absence of pure dephasing ($T_2 = 2T_1$), the relation of p_0 and p_1 with excitation power can readily be estimated through steady-state equilibrium. We define $\bar{n}$ as the mean incident photon number over T_1 duration[11], and η_{ab} as the TLE's absorption efficiency under weak excitation limit. With absorption balancing out emission, we obtain $\frac{\bar{n}}{T_1} \times \eta_{ab} \times (1-p_1) = \frac{p_1}{2} \times \frac{1}{T_1}$, where the factor $(1-p_1)$ on the left takes saturation into account while $\frac{p_1}{2}$ on the right reflects on average only half of the excited state is in the matter form. We then have

$$\begin{aligned} p_0 &= \frac{1}{1+2\bar{n}\eta_{ab}},\\ p_1 &= \frac{2\bar{n}\eta_{ab}}{1+2\bar{n}\eta_{ab}}. \end{aligned} \tag{4}$$

These equations connect p_0 and p_1 directly to the single photon excitation level, and are applicable to both Heitler and Mollow excitation regimes. Since no assumption is made on the emitter type, Eq. (4) holds, under the condition $T_2 = 2T_1$, for all quantum two-level emitters, including a trapped atom[8,10] or ion[12], a molecule[22], and a semiconductor QD[13–16,23,24]. The absorption efficiency η_{ab} may vary drastically among emitters, but embedding an emitter into a cavity can enhance the light-matter interaction and could bring η_{ab} close to unity. For a high-quality QD-micropillar device[11,25,26], we expect $|g^{(1)}(\tau)| = p_0 \simeq \frac{1}{1+2\bar{n}}$, which presents a unique test-point to our model.

Equation (2) yields another experimentally verifiable prediction. Looking at the third line of this equation, the laser-like component, though being dominant under weak excitation, can be completely eliminated through destructive interference by setting the AMZI phase to $\varphi = \pi$. Containing only the non-interfering single-photon term ($|0_c 1_d\rangle_t (|ge\rangle - |eg\rangle)$) and a photon-pair term ($|0_c 2_d\rangle_t |gg\rangle$), the output at port d closely resembles the result of passing a photonic state composed solely of vacuum and two-photon terms, $(1-\frac{p_1^2}{2})|0\rangle\langle 0| + \frac{p_1^2}{2}|2\rangle\langle 2|$, through a beam splitter. Naturally, the port d output with $\varphi = \pi$ will exhibit excitation-flux-dependent super-bunching, as derived in Section V of the Supplementary Information:

$$g^{(2)}(0) = \frac{1}{p_1^2} = \left(1 + \frac{1}{2\bar{n}\eta_{ab}}\right)^2. \tag{5}$$

At low pump limit ($\bar{n} \rightarrow 0$), the $g^{(2)}(0)$ value can theoretically be infinitely large. At the opposite limit ($\bar{n} \rightarrow \infty$), the RF loses all its first-order coherence according to Eq. (3) and the super-bunching disappears, i.e., $g^{(2)}(0) = 1$. We remark that the predicted super-bunching is not observable with an incoherently pumped TLE.

Excitation-power dependence of the first-order coherence

To test, we use a QD-micropillar device[11] featuring a quality factor of 9350 and a low cavity reflectivity of 0.015. It is kept in a closed-cycle cryostat and the QD's neutral exciton is temperature-tuned into the cavity resonance at 13.6 K, emitting at 911.54 nm. The setup is schematically shown in Fig. 1b. We use a confocal microscope setup equipped with a tunable continuous-wave (CW) laser of 100 kHz linewidth as the excitation source and an optical circulator made of a polarising beam splitter and a quarter-wave plate for collecting the RF in the same polarisation of the driving laser[11,27]. The QD is characterised to have a Purcell enhanced lifetime of $T_1 = 67.2$ ps ($F_p \simeq 10$), corresponding to a natural linewidth of $\gamma_{\parallel}/2\pi = 2.37$ GHz, which is 15 times narrower than the cavity mode ($\kappa/2\pi = 35$ GHz). The RF is fed into a custom-built AMZI with a fixed delay of $\tau = 4.92$ ns for interference before detection by single photon detectors. With additional apparatuses, the whole setup allows characterisations of high-resolution spectroscopy, auto-correlation function $g^{(2)}(\Delta t)$, the first-order correlation function $g^{(1)}(\tau)$, and two-photon interference. All excitation fluxes used were strictly calibrated via the incident optical power (P_{in}) upon the sample surface using the relation of $\bar{n} = P_{in} T_1/h\nu$. Detailed description of the experimental setup can be found in "Methods".

In the first experiment, we use a weak excitation flux of $\bar{n} = 0.0068$, corresponding to a Rabi frequency of $\Omega/2\pi = 210$ MHz ($\sim 0.09\gamma_{\parallel}$). Figure 1c shows the auto-correlation function $g^{(2)}(\Delta t)$ for both the RF (orange line) and the laser (blue line). While the laser exhibits a flat $g^{(2)}$ because of its Poissonian statistics, the RF is strongly anti-bunched, with $g^{(2)}(0) = 0.024 \pm 0.002$, at the 0-delay over a timescale of $\sim T_1$, confirming that the QD scatters one photon at a time.

Figure 1d shows the RF frequency spectrum (orange line) measured with a scanning Fabry-Pérot interferometer (FPI). It is dominated by a sharp line that overlaps the laser spectrum (blue line) with a linewidth that is limited by the FPI resolution (20 MHz). The RF contains additionally a broadband pedestal whose amplitude is over 3

https://doi.org/10.1038/s41467-025-61884-x

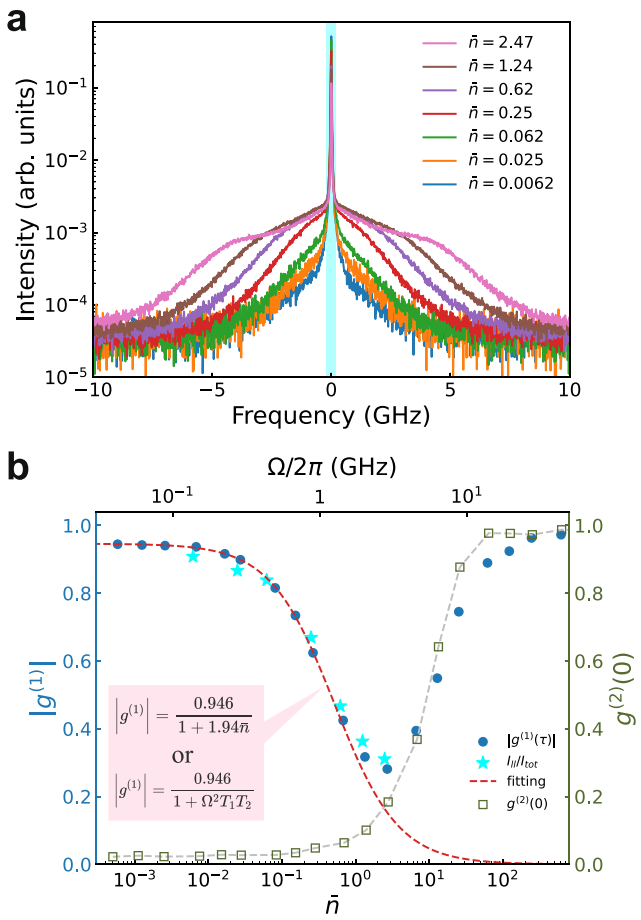

Fig. 2 | Coherence versus incident flux. a High-resolution spectra; The cyan bar illustrates the laser-like spectral part. **b** $|g^{(1)}|$ (solid circles) measured with the AMZI and $I_{\parallel}/I_{tot}$ (solid stars) extracted from data in (**a**), as well as $g^{(2)}(0)$ measured without any spectral filtering. The red dashed line is a fitting using either $|g^{(1)}| \propto \frac{1}{1+x\bar{n}}$ with $x = 1.94$ or $|g^{(1)}| \propto \frac{1}{1+\Omega^2 T_1 T_2}$ with $T_2 = 1.62T_1$.

orders of magnitude weaker. The overall spectrum can be excellently fit with two Lorentzians of 20 MHz and 2.3 GHz linewidths, shown as cyan and black dashed lines, respectively. The bandwidth of the latter closely matches the TLE's natural linewidth of $\gamma_{\parallel}/2\pi$. Following the discussion surrounding Eq. (3), we attribute the sharp feature to the interference outcome of the RF signal passing through the FPI. The spectral weight of this laser-like peak can be measured using our AMZI (Fig. 1b), whose delay meets the steady-state condition $T_1 \ll \tau \ll T_L$. An example result is shown in Fig. 1e, which gives a fringe visibility, or the laser-like fraction, of 0.94 for the RF. As comparison, the laser signal exhibits 0.9998 interference visibility.

Figure 2a shows high-resolution RF spectra under different excitation fluxes. As the flux increases, the broadband component increases its share of the total RF, and becomes considerably broadened when $\bar{n}$ exceeds 0.25. It starts to develop into Mollow triplets at the few photon level as reported previously[11]. Nevertheless, the RF retains its single-photon characteristics for a flux up to $\bar{n} = 6.8$ when measured before the AMZI and without any spectral filtering, as demonstrated by the auto-correlation data (open squares) in Fig. 2b. At $\bar{n} = 6.8$, we measure $g^{(2)}(0) = 0.37$, which is still below the limit (0.5) for a classical emitter.

The growing broadband component deteriorates the RF's coherence. To quantify, we measure the interference visibility ($|g^{(1)}|$) by passing the RF through the AMZI, with results shown as solid circles in Fig. 2b. This quantification method is equivalent to, and more precise than, calculating the area ratio of the laser-like peak to the total RF signal. The results from the latter method are shown as stars. At low fluxes ($\bar{n} < 0.01$), $|g^{(1)}|$ is plateaued at 0.946, rather than 1.0 as expected from Eq. (3). We attribute this discrepancy to photon distinguishability[28], which could arise from phonon-scattering[29–31] and QD environmental charge fluctuation[32] as well as a small amount of laser mixed into the RF. As the flux increases until $\bar{n} = 3$, we observe a general trend of a decreasing visibility. For $\bar{n} > 3.0$, the visibility reverses its downward trend and climbs up. In this regime, the RF signal starts to saturate[11] while the laser background continues to rise, as evidenced by the accompanying rise in $g^{(2)}(0)$. At very strong fluxes ($\bar{n} > 100$), the laser background dominates because our setup collects the RF in the same polarisation of the driving laser, and thus the measured photon number statistics approaches Poissonian distribution, i.e., $g^{(2)}(0) \approx 1$.

We attribute the interference visibility drop in Fig. 2b to the increasing population (p_1) of the QD's exited state. Based on Eqs. (3) and (4), we obtain a near perfect fit, $|g^{(1)}| = 0.946/(1+x\bar{n})$ and $x = 1.94$, to the experimental data in the region where the RF signal remains dominant. The fitting is identical to the result (also shown as dashed line) by the traditional model[3,13,26]: $|g^{(1)}| \propto \frac{1}{1+\Omega^2 T_1 T_2}$, where we use $T_2 = 1.62T_1$ and the Rabi frequencies extrapolated from the Mollow splittings measured under strong excitations. This is unsurprising because both models share the same theoretical foundation and $\bar{n} \propto \Omega^2$ holds. However, our model gives a more direct link of the RF's coherence to the excitation power, without the need for extracting the Rabi frequencies in order to achieve so. This experiment strongly supports our model and at the same time suggests an efficient input-coupling of our QD-micropillar device with $\eta_{ab} \simeq 0.97$.

Photon super-bunching

In the next experiment (Fig. 3a), we use the AMZI to filter out the laser-like component by setting its phase to $\varphi = \pi$ and then examine the super-bunching as expected in Eq. (4). As compared with a narrow-band filter[6–8], this technique uses two-path, instead of multi-path, interference and thus the subsequent photon number statistics is easier to analyse. For the theoretical analysis, see Section V of Supplementary Information. Two AMZI-filtered spectra are shown in Fig. 3b. Each spectrum consists of a broadband signal with interference fringes of 203 MHz spacing corresponding to the AMZI's delay ($\tau = 4.92$ ns), while the laser-like component is rejected entirely. Subjecting the filtered RF to the auto-correlation measurement, we acquire a set of data shown in Fig. 3c. We observe super-bunching at 0-delay with $g^{(2)}(0) = 168.9$ at the lowest flux of $\bar{n} = 0.0062$. At $\Delta t = \pm\tau$, interference between three temporal modes happens. Theoretically, $g^{(2)}(\pm\tau) \approx \frac{1}{4}g^{(2)}(0)$ under such incident flux. To compare, we have measured an average value of 47.6 for $g^{(2)}(\pm\tau)$, amounting to 0.282 of the corresponding $g^{(2)}(0)$ value.

We attribute the observed super-bunching to a combined effect of two-photon interference and the RF's first-order destructive interference. The former generates two-photon states contributing to the 0-delay coincidences, while the latter reduces the photon intensity in the AMZI output port and thus suppresses the coincidence baseline. Setting $\varphi = \pi$ maximises the level of super-bunching, but $g^{(2)}(0)$ can be tuned continuously down to anti-bunching through the AMZI phase. Details about AMZI phase stabilisation and measurements for other characteristic phases are shown in "Methods".

As the excitation flux increases, we expect the RF's first-order coherence to reduce and so will the level of super-bunching. Figure 3c shows the excitation flux dependence of the auto-correlation, which is in qualitative agreement with the theoretical prediction of Eq. (4). At $\bar{n} = 0.62$, we deduce $p_1 = 0.546$ using the empirical relation of $p_1 = 1.94\bar{n}/(1+1.94\bar{n})$ and thus expect a photon bunching value of 3.35. Experimentally, we obtain $g^{(2)}(0) = 2.6$, which is in fair agreement with

https://doi.org/10.1038/s41467-025-61884-x

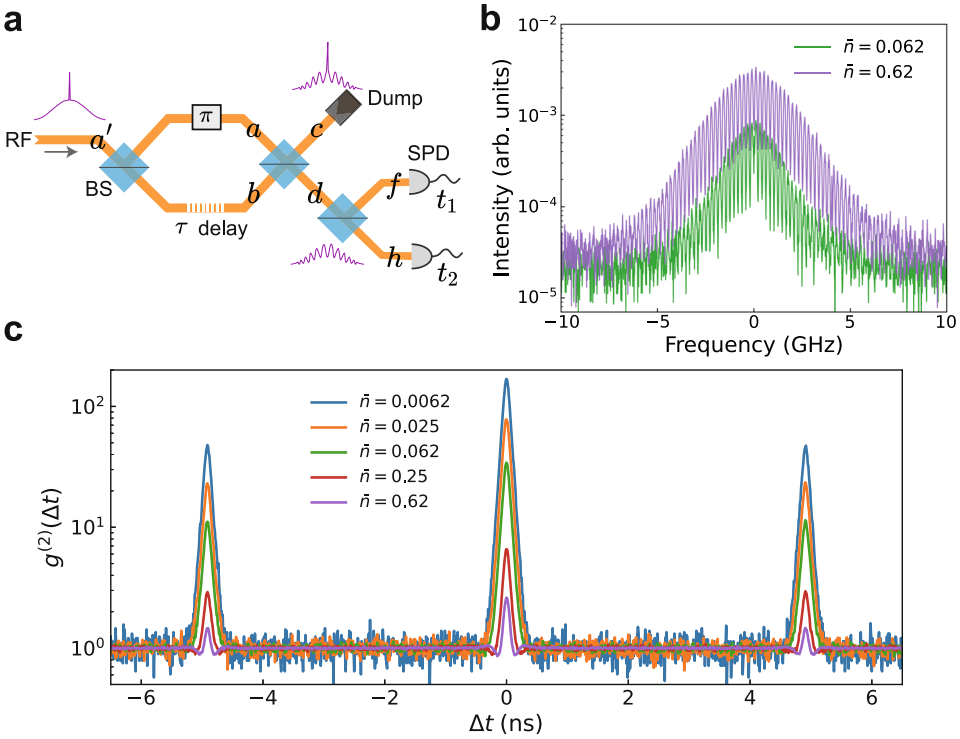

Fig. 3 | Correlation of the AMZI-filtered RF. a Experimental setup; The AMZI is set to have a π phase so that the laser-like RF component is dumped at port *c*; The filtered RF at port *d* contains only the broadband component, and is fed into a HBT setup. **b** Filtered RF spectra; **c** Second-order correlation functions measured for various excitation fluxes.

the expected value. The discrepancy could arise from the increased laser background as well as finite photon indistinguishability[28].

Phase-dependent two-photon interference

Finally, we perform phase-dependent two-photon interference experiment with the setup shown in Fig. 1b, and summarise the results in Fig. 4a with observations: (1) The coincidence baseline is phase-dependent, while the gap between traces shrinks as the excitation power increases; (2) Strong anti-bunching at $\Delta t = 0$ for all excitation fluxes and phase values; (3) Features at $\Delta t = \pm 4.92$ ns, caused by the AMZI's delay τ, can exhibit as peaks or dips depending on both the excitation power and the phase delay. We note that observation (3) is strikingly different from incoherently excited quantum emitters[26,33], where the side features always display as dips with depth limited to 0.75.

To understand the two-photon interference results, we approximate the RF output as a superposition of photon-number states: $|\psi_{ph}\rangle_t = \sqrt{p_0}|0\rangle_t + \sqrt{p_1}|1\rangle_t + \sqrt{p_2}|2\rangle_t$ with a small two-photon probability $p_2 \ll p_1^2/2$ and derive the coincidence probabilities as detailed in Section VI of Supplementary Information. We reproduce the main results below.

$$\mathcal{C}(0) = \frac{p_2}{4}\left(1 - p_0 M \cos 2\varphi\right) + \frac{p_1^2 + 4p_1p_2 + 4p_2^2}{8}(1 - M'), \tag{6}$$

$$\mathcal{C}(\pm\tau) = \frac{p_1^2}{16}(3 - 2p_0 M \cos 2\varphi), \tag{7}$$

$$\mathcal{C}_0 = \frac{p_1^2}{4}\left(1 - p_0^2 M \cos^2\varphi\right), \tag{8}$$

where M represents indistinguishability of the RF photons while M' is the post-selective two-photon interference visibility with detector jitter taken into account[34]. $\mathcal{C}(\Delta t)$ represents the coincidence probability at time interval Δt while $\mathcal{C}_0$ is the baseline coincidence. Equations (6)–(8) show all coincidence probabilities are phase-dependent. $\mathcal{C}_0$ and $\mathcal{C}(\pm\tau)$'s dependence arises from the first-order interference, while $\mathcal{C}(0)$ contains contributions from $|2\rangle_t$ states as well as incomplete HOM interference between two RF photons emitted separately by the AMZI delay τ. Figure 4b, c plots the phase dependence of the theoretical (solid lines) and experimental (symbols) coincidence rates for $\Delta t = \pm\tau$ and $\Delta t = 0$, normalised to the baseline coincidence. We use maximum likelihood estimation method to determine a realistic set of parameters for each excitation flux that provide the best fit to the data. The theoretical simulations are in excellent agreement with the experimental data for three incident fluxes and have also successfully reproduced the crossover between $\mathcal{C}(\pm\tau)$ and $\mathcal{C}_0$ for $\bar{n} = 0.25$.

Discussion

Over past 50 years, it has been prevalent to discuss resonance fluorescence in the context of "coherently" and "incoherently" scattered light[5–9,13,14,20]. In literature, interchangeable terminologies, such as resonant Rayleigh scattering (RRS) vs. resonant photoluminescence (RPL)[26] and elastic vs. inelastic scattering[35], are also in use. The term "incoherent scattering" is rather misleading. As we have elucidated, both the laser-like and broadband parts arise from the very same coherent process, i.e., resonant absorption and spontaneous emission. The two parts are integral. Their integrity is key to the joint observation of "sub-natural" linewidth and anti-bunching. Conversely, compromise in the integrity will change the photonic state and may lead to different observations, e.g., loss of anti-bunching after spectral filtering[6–8] or super-bunching after the AMZI filtering (Fig. 3). We stress that photon bunching does not necessarily require simultaneous scattering of two photons[8] for an explanation.

https://doi.org/10.1038/s41467-025-61884-x

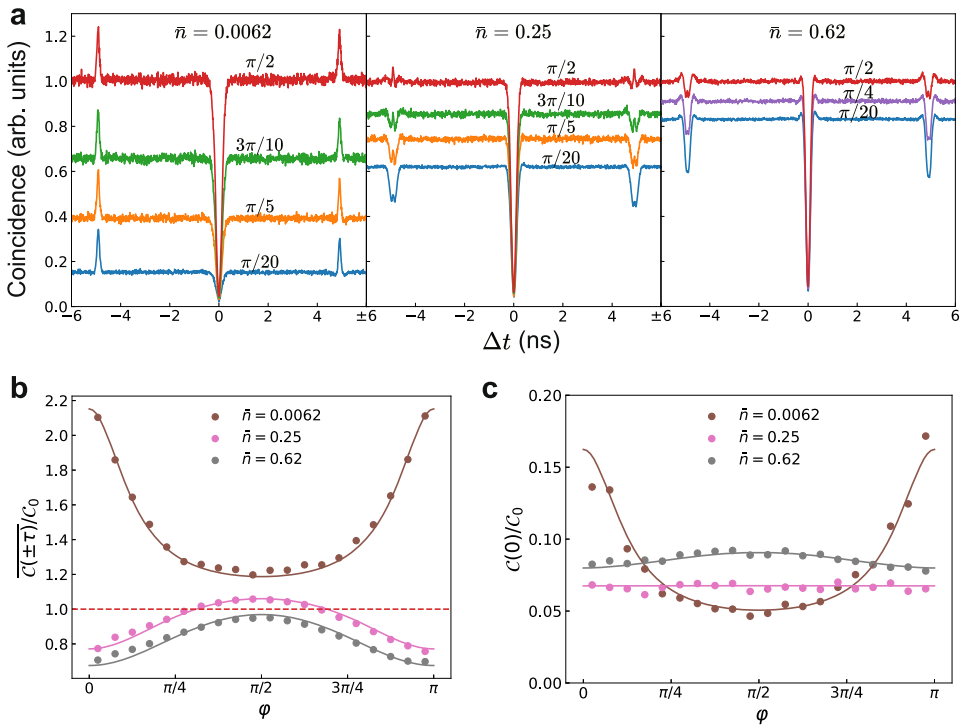

Fig. 4 | Phase-dependent two-photon interference. a Cross-correlation traces measured with the setup shown in Fig. 1b for three different excitation intensities: $\bar{n} = 0.0062$ (left), 0.25 (middle) and 0.62 (right panel). **b** Measured (solid symbols) and theoretical (solid lines) coincidence probabilities at $\Delta t = \pm\tau$ delays, normalised to the coincidence baseline (dashed line). We use $\overline{C(\pm\tau)} = \frac{1}{2}(C(+\tau) + C(-\tau))$. **c** Normalised experimental (solid symbols) and theoretical (solid lines) coincidence probabilities at $\Delta t = 0$. Experimental data in **b** and **c** are extracted from data in (**a**). The theoretical results are fitted using maximum likelihood estimation. Fitted parameters $\{p_0, p_1, p_2; M'\}$ corresponding to different excitation fluxes $\bar{n} = 0.0062, 0.25, 0.62$ are $\{0.98, 0.023, 8.0 \times 10^{-6}; 0.96\}$, $\{0.69, 0.30, 2.2 \times 10^{-3}; 0.94\}$ and $\{0.49, 0.50, 8.0 \times 10^{-3}; 0.92\}$, respectively. A fixed value of $M = 0.89$, extracted from the plateaued $|g^{(1)}| = 0.946$ shown in Fig. 2b through $M = |g^{(1)}|^2$, is used for photon indistinguishability.

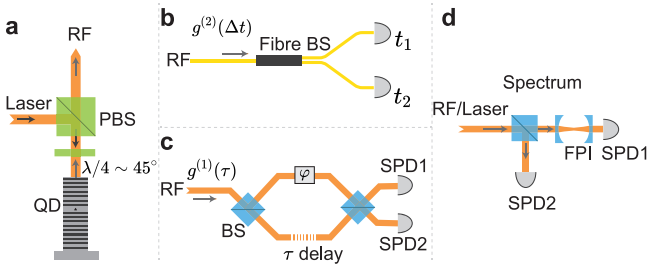

Fig. 5 | Experimental setup. a Confocal RF; **b** HBT; **c** AMZI for $g^{(1)}(\tau)$ measurement; **d** High-resolution spectral measurement.

To conclude, we have presented a unified model to explain the coherence of resonance fluorescence under continuous-wave excitation. It links the RF's coherence to the incident flux down to the single-photon level and we show how to manipulate photon number statistics through simple two-path interference. We clarify that coherent scattering can be treated as a process of absorption and re-emission and does not need to involve higher-order scattering processes[8] to explain experiments. Our work adds clarity to the knowledge pool of RF-based quantum light sources and we believe it will help foster new applications. One opportunity is to exploit the RF's coherence for quantum secure communication[36,37].

Methods

Experimental setup

The main RF setup is shown in Fig. 5a. Here, a polarising beam splitter (PBS) and a ~45° quarter-wave plate are used together as an optical router to direct the RF from the QD to the measurement apparatuses shown in panels b, c and d. A CW laser (~100 kHz linewidth) is used as the excitation source. Although the reflected laser and the RF have the same polarisation, contamination from the former is minimal due to the cavity's ultra-low reflectivity of 0.015 at the resonance wavelength. Figure 5b shows a standard Hanbury Brown-Twiss (HBT) setup for measuring the auto-correlation function $g^{(2)}(\Delta t)$ that evaluates the single-photon purity of the input signal. It consists of a 50:50 fibre beam splitter and two single photon detectors.

Figure 5c illustrates a setup for characterising the first-order correlation function $g^{(1)}(\tau)$. In this setup, both beam splitters have a nominal 50:50 reflectance-to-transmittance ratio, and the AMZI's differential delay is 4.92 ns. The count rates at the detectors oscillate with a free-drifting phase φ. By measuring the maximum and minimum values of this oscillation, we can calculate the interference fringe visibility: $V \equiv |g^{(1)}(\tau)| = \frac{C_{max} - C_{min}}{C_{max} + C_{min}}$. Usually, one detector would suffice. However, to avoid the QD blinking affecting the measurement result, we use a two-channel summation method to normalise each detector's count rate to the combined count rate for the visibility calculation.

In measuring the high resolution RF spectra, we use a setup shown in Fig. 5d. The signal is split into two paths. One path enters the scanning FPI with a single photon detector (SPD1) recording the signal count rate as a function of the FPI transmission frequency which is controlled by a piezo actuator. The other path enters a second single photon detector (SPD2) for normalising SPD1's detection results. The scanning FPI has a free spectral range of 20 GHz and a resolution of 20 MHz.

Two superconducting nanowire single photon detectors (SNSPDs) are used and characterised to have a detection efficiency of 78% and a time jitter of 48 ps at a wavelength of 910 nm. A time-tagger is used for correlation and time-resolved measurements.

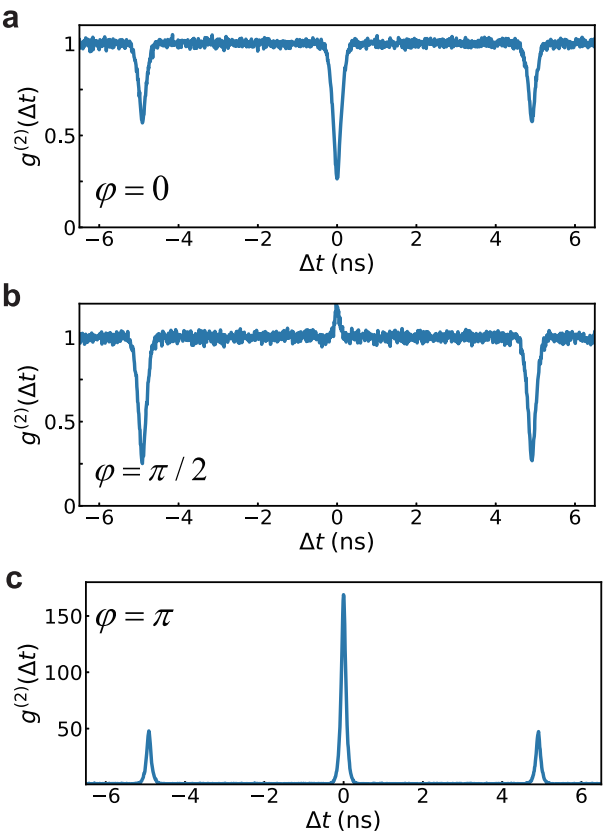

Fig. 6 | Phase-dependent auto-correlation of the AMZI-filtered RF. The excitation flux is set at $\bar{n} = 0.0062$. **a** $\varphi = 0$; **b** $\varphi = \pi/2$; **c** $\varphi = \pi$.

Phase-locking the AMZI

The AMZI is made from optical fibres and sealed in an enclosure to shield from external airflow and ambient temperature fluctuation. However, its phase still drifts on the order of π per minute. While adequate for the first-order coherence measurement (e.g., see Fig. 1c), this level of stability does not meet the requirement by our phase-dependent correlation experiments. To eliminate the phase drift, we use a thermo-electric cooler to actively control the internal temperature of the enclosure, based on the ratio of the single-photon counting rates between the AMZI outputs.

While having been demonstrated in Figs. 3 and 4, the effectiveness of the phase-locking can be further appreciated from the phase-dependent auto-correlation data shown in Fig. 6. Using the setup shown in Fig. 3a, the photon correlation statistics of the AMZI-filtered RF signal can be tuned from anti-bunching ($g^{(2)}(0) < 1$) at $\varphi = 0$ to super-bunching ($g^{(2)}(0) \gg 1$) at $\varphi = \pi$. The result is consistent with our theoretical calculation, where we obtain $g^{(2)}(0) \equiv \frac{\mathcal{C}(0)}{\mathcal{C}_0} = \frac{1}{(1+p_0\cos\varphi)^2}$ with $\mathcal{C}(0) = p_1^2/16$ and $\mathcal{C}_0 = (1+p_0\cos\varphi)^2 p_1^2/16$ being the 0-delay and baseline coincidence probabilities, respectively.

Data availability

The data that support the plots within this paper are deposited on Zenodo[38].

References

1. Scully, M. O. & Zubairy, M. S. *Quantum Optics* (Cambridge University Press, 1997).
2. Mandel, L. & Wolf, E. *Optical Coherence and Quantum Optics* (Cambridge University Press, 1995).
3. Loudon, R. *The Quantum Theory of Light* (OUP Oxford, 2000).
4. Steck, D. A. Quantum and atom optics, http://steck.us/teaching (2023).
5. López Carreño, J. C., Zubizarreta Casalengua, E., Laussy, F. P. & del Valle, E. Joint subnatural-linewidth and single-photon emission from resonance fluorescence. *Quant. Sci. Technol.* **3**, 045001 (2018).
6. Phillips, C. L. et al. Photon statistics of filtered resonance fluorescence. *Phys. Rev. Lett.* **125**, 043603 (2020).
7. Hanschke, L. et al. Origin of antibunching in resonance fluorescence. *Phys. Rev. Lett.* **125**, 170402 (2020).
8. Masters, L. et al. On the simultaneous scattering of two photons by a single two-level atom. *Nat. Photon.* **17**, 972–976 (2023).
9. Casalengua, E. Z., Laussy, F. P. & del Valle, E. Two photons everywhere. *Phil. Trans. R. Soc. A* **382**, 20230315 (2024).
10. Ng, B. L., Chow, C. H. & Kurtsiefer, C. Observation of the Mollow triplet from an optically confined single atom. *Phys. Rev. A* **106**, 063719 (2022).
11. Wu, B. et al. Mollow triplets under few-photon excitation. *Optica* **10**, 1118 – 1123 (2023).
12. Höffges, J., Baldauf, H., Eichler, T., Helmfrid, S. & Walther, H. Heterodyne measurement of the fluorescent radiation of a single trapped ion. *Opt. Commun.* **133**, 170–174 (1997).
13. Nguyen, H.-S. et al. Ultra-coherent single photon source. *Appl. Phys. Lett.* **99**, 261904 (2011).
14. Konthasinghe, K. et al. Coherent versus incoherent light scattering from a quantum dot. *Phys. Rev. B* **85**, 235315 (2012).
15. Matthiesen, C., Vamivakas, A. N. & Atatüre, M. Subnatural linewidth single photons from a quantum dot. *Phys. Rev. Lett.* **108**, 093602 (2012).
16. Matthiesen, C. et al. Phase-locked indistinguishable photons with synthesized waveforms from a solid-state source. *Nat. Commun.* **4**, 1600 (2013).
17. Carmichael, H. J. & Walls, D. F. Proposal for the measurement of the resonant stark effect by photon correlation techniques. *J. Phys. B At. Mol. Opt. Phys.* **9**, L43 (1976).
18. Kimble, H. J., Dagenais, M. & Mandel, L. Photon antibunching in resonance fluorescence. *Phys. Rev. Lett.* **39**, 691–695 (1977).
19. Lodahl, P., Mahmoodian, S. & Stobbe, S. Interfacing single photons and single quantum dots with photonic nanostructures. *Rev. Mod. Phys.* **87**, 347–400 (2015).
20. Mollow, B. R. Power spectrum of light scattered by two-level systems. *Phys. Rev.* **188**, 1969–1975 (1969).
21. Hong, C. K., Ou, Z. Y. & Mandel, L. Measurement of subpicosecond time intervals between two photons by interference. *Phys. Rev. Lett.* **59**, 2044–2046 (1987).
22. Wriggle, G., Gerhardt, I., Hwang, J., Zumofen, G. & Sandoghdar, V. Efficient coupling of photons to a single molecule and the observation of its resonance fluorescence. *Nat. Phys.* **4**, 60–66 (2008).
23. Ates, S. et al. Post-selected indistinguishable photons from the resonance fluorescence of a single quantum dot in a microcavity. *Phys. Rev. Lett.* **103**, 167402 (2009).
24. Flagg, E. B. et al. Resonantly driven coherent oscillations in a solid-state quantum emitter. *Nat. Phys.* **5**, 203–207 (2009).
25. De Santis, L. et al. A solid-state single-photon filter. *Nat. Nanotech.* **12**, 663–667 (2017).
26. Proux, R. et al. Measuring the photon coalescence time window in the continuous-wave regime for resonantly driven semiconductor quantum dots. *Phys. Rev. Lett.* **114**, 067401 (2015).
27. Bennett, A. et al. A semiconductor photon-sorter. *Nat. Nanotech.* **11**, 857–860 (2016).
28. Loredo, J. et al. Generation of non-classical light in a photon-number superposition. *Nat. Photon.* **13**, 803–808 (2019).
29. Iles-Smith, J., McCutcheon, D. P. S., Nazir, A. & Mørk, J. Phonon scattering inhibits simultaneous near-unity efficiency and

indistinguishability in semiconductor single-photon sources. *Nat. Photon.* **11**, 521–526 (2017).
30. Koong, Z. X. et al. Fundamental limits to coherent photon generation with solid-state atomlike transitions. *Phys. Rev. Lett.* **123**, 167402 (2019).
31. Brash, A. J. et al. Light scattering from solid-state quantum emitters: beyond the atomic picture. *Phys. Rev. Lett.* **123**, 167403 (2019).
32. Zhai, L. et al. Low-noise GaAs quantum dots for quantum photonics. *Nat. Commun.* **11**, 4745 (2020).
33. Patel, R. B. et al. Postselective two-photon interference from a continuous nonclassical stream of photons emitted by a quantum dot. *Phys. Rev. Lett.* **100**, 207405 (2008).
34. Legero, T., Wilk, T., Hennrich, M., Rempe, G. & Kuhn, A. Quantum beat of two single photons. *Phys. Rev. Lett.* **93**, 070503 (2004).
35. Metcalfe, M., Solomon, G. S. & Lawall, J. Heterodyne measurement of resonant elastic scattering from epitaxial quantum dots. *Appl. Phys. Lett.* **102**, 231114 (2013).
36. Zhou, L. et al. Experimental quantum communication overcomes the rate-loss limit without optical phase tracking. *Phys. Rev. Lett.* **130**, 250801 (2023).
37. Karli, Y. et al. Controlling the photon number coherence of solid-state quantum light sources for quantum cryptography. *npj Quant. Inf.* **10**, 17 (2024).
38. Wang, X.-J. et al. Data accompanying "Coherence in resonance fluorescence", https://doi.org/10.5281/zenodo.15717876 (2025).

Acknowledgements

The authors thank Z. Q. Yin, Y. K. Wu, Y. Ji, X. B. Wang and C. Antón-Solanas for helpful discussions and S. Wein for help on derivation of Eq. (1). This work was supported by Beijing Natural Science Foundation under grant IS23011 (Z.Y.), the National Natural Science Foundation of China under grants 12204049 (X.-J.W.), 12494604 (Z.Y.), 62250710162 (Z.Y.) and 12274223 (H.-L.Y.), National Key R&D Program of China under grant 2018YFA0306101 (Z.N.) and the Fundamental Research Funds for the Central Universities and the Research Funds of Renmin University of China under grant 24XNKJ14) (H.-L.Y.).

Author contributions

Z.Y., X.-J.W. and B.W. designed the research. X.-J.W., G.H. and B.W. carried out the experiments. H.-L.Y., M.-Y.L., Y.-Z.W. and X.-J.W. developed the theoretical derivation and performed the simulations. L.L. fabricated the devices with assistance from W.J. H.L., H.N. and Z.N. grew the semiconductor wafer. X.-J.W. and Z.Y. prepared the manuscript with input from R.J. and other authors. Z.Y. conceived the model and supervised the project.

Competing interests

The authors declare no competing interests.

Additional information

Supplementary information The online version contains supplementary material available at https://doi.org/10.1038/s41467-025-61884-x.

Correspondence and requests for materials should be addressed to Bang Wu, Hua-Lei Yin or Zhiliang Yuan.

Peer review information *Nature Communications* thanks the anonymous reviewer(s) for their contribution to the peer review of this work. A peer review file is available.